EDUCING COHERENT EDDY STRUCTURES IN AIR CURTAIN SYSTEMS

Karine Loubière[1] and Michel Pavageau[2(*)]

GEPEA UMR 6144 CNRS/Université de Nantes/ENITIAA/Ecole des Mines de Nantes

[1] CRTT - BP 406, 44602 Saint-Nazaire Cedex, France

[2] Ecole des Mines de Nantes, Département Systèmes Energétiques et Environnement,

4 rue Alfred Kastler, BP 20722, 44 307 Nantes Cedex 3, France.

(*) Corresponding author. Tel. +33 2 51 85 82 67; Fax +33 2 51 85 82 99; E-mail address: pavageau@emn.fr

Abstract

The work reported here comes within a broader research program dealing with ambiance separation or confining by means of air curtains (plane air jets). The process is studied experimentally by Particle Image Velocimetry (PIV). In this paper, the emphasis is put on the flow structure in the impingement region of such jet systems insofar as it is where transfers occur preferentially. More precisely, a vortex eduction method was implemented under the Matlab environment enabling both the automatic detection of 2D coherent patterns embedded in PIV velocity vector maps, and a statistical analysis of the topological and energy features of these structures. First, the approach is explained in detail. The second part of this paper is devoted to its application in the case of plane turbulent impinging simple- and twin-jets for various jet exit velocities. Results about the size, the shape, the spatial distribution and the energy content of the detected vortices are provided. Although many questions still remain open, new insights into the fashion these structures might form, organize and evolve are given providing an original picture of the plane turbulent impinging jet.

1. Introduction

Air curtains are separation devices based on the discharge of a plane air stream to isolate from each other two adjacent air volumes with different climatic characteristics (in the broad sense of the term). The jet system provides a fluid seal against heat, moisture and/or mass transfers between the separated areas without holding up traffic of people, vehicles, materials or objects. Thus, air curtains are particularly useful in situations where conventional physical barriers become unacceptable for practical, technical, economical or safety reasons. The applications for air curtains are many. They include, but are not limited to air conditioned areas, commercial entrances, refrigerated counters, clean rooms, testing chamber apparatus (e.g. thermal shock test chambers), industrial oven openings, tunnel fire safety systems, process line partitioning in the food or microelectronics industry, etc…[1-8].

Most of the time, air-curtains consist of one or several jets blown vertically or obliquely downwards. After the jet hits the floor, the supplied air simply spills into the regions on either side of the jet (Fig. 1a). In many cases, the geometrical aspect ratio of the rectangular discharge nozzle is such that air curtains may be regarded as two-dimensional plane jets. Furthermore, discharge air velocities commonly encountered in conventional devices are of the order of a few meters per second. Thus, in more academic terms, air curtains can be viewed as plane turbulent impinging jets.

The sealing efficiency of an air curtain is directly related to the amount of ambient fluid particles entrained into the main flow and carried across it by convection and diffusion. It can never reach 100%. In this respect, it is obvious that the Kelvin-Helmholtz-like instabilities that develop in the shear layers along the lateral boundaries of the jet flow (Fig. 1a) play a relevant role. However, LES simulations [9] have shown that it is in the impingement region (Fig. 1a) where mass transfer across the jet stream preferentially occurred. This seems to be strongly related to the presence of large-scale organized motions appearing in the form of

elongated roll cells whose main axis is roughly perpendicular to the jet plane (Fig. 1b). Also detected experimentally by [10-12], these tubular structures are accelerated and stretched longitudinally by the impingement wall flows developing on either part of the jet after hiting the floor. It has been shown that they were characterized locally by a strong vortical intensity and a noticeable energy content.

Consequently, in place of or in addition to a passive or active control of the growth of the instabilities developing in the lateral mixing layers of a jet [13-17], it may be interesting to act on the flow structure in the impingement region so as to improve the efficiency of air curtains. However, before working out appropriate solutions, it is necessary to better understand the fashion in which the large-scale structures present in the impingement region of a jet form, evolve and contribute to transfer mechanisms. From this, an algorithm was developed to automate the identification of vortical patterns embedded in instantaneous velocity vector maps obtained by standard 2D particle image velocimetry (PIV). Structures are characterized topologically and with respect to the energy they carry. Analysis is performed on series of instantaneous velocity fields: relevant results are returned mainly in the form of probability density functions (pdf) of the observed quantities. Since our PIV measurements are not time resolved, the temporal coherence of the detected structures cannot be verified.

The paper is organized as follows. Section 2 provides a description of the main steps of the above mentioned algorithm. After a description of the experimental set-up, the test configurations and the PIV measurements, the observations made for various air-curtain arrangements and jet exit velocities are examined in Section 3. Finally, in Section 4, conclusions will be drawn and perspectives will be outlined.

2. Automatic method for eddy structure eduction and characterisation

Due to the diversity and the complexity of flows where coherent structures are embedded, no consensual and general definition of a such structures is yet established [18]. Nevertheless, it is agreed that they refer to large-scale organized swirling motions and that, during their transport, they should exhibit a certain degree of integrity over certain spatial and temporal scales [19-21]. Their separation from background turbulence does not rely on one unique and systematic method. The technique used to determine when and where certain structures are passing or present is directly related to the definition adopted for these structures. In the literature, a multitude of techniques are available (see the general overview of Bonnet et al (1998) [22]). The choice of one particular method is generally conditioned by the desired information, by the way the structure is defined, but also by the experimental and numerical capabilities available.

Particle Image Velocimetry (PIV) as a whole-field measurement technique has open interesting perspectives with respect to pattern recognition in turbulent flows [23-24]; indeed, flow maps with a spatial resolution close to the resolution achieved numerically are now accessible more easily than with pointwise measurement techniques. Thus, the standard PIV provides an amount of information sufficient enough to make possible the educing of large coherent eddy structures even though a two-dimensional description of the flow field and a poor temporal resolution cannot supply all the characteristics of basically three-dimensional coherent structures. The amount of data produced requires automation for post-processing procedures of instantaneous field series. For this purpose, we developed an algorithm enabling the detection and characterization of coherent 2D-patterns embedded in PIV velocity maps automatically. Its implementation under the Matlab environment was concerned about minimizing subjective intervention of the user so as to derive as unbiased statistics as possible. The main steps of our method are presented hereafter. Many more

details can be found in [25].

2.1 *Preliminary calculations*

Structure identification methods require the computation of spatial derivatives of the fluid velocity. Therefore, a certain continuity and smoothness of the velocity fields under study must be ensured. However, PIV measurements are discrete in space, with a relative spatial resolution usually much below than the numerical resolution. They additionally contain a certain amount of noise, the high frequency component of which must be removed or at least damped prior to the calculation of the spatial derivatives of velocity.

Therefore, a low-pass two-dimensional homogeneous Gaussian filter is chosen to smooth instantaneous PIV velocity fields. The filter window was set equal to 7×7 grid spacings. Not justified here, this choice comes from a complete and detailed sensitivity analysis [25] whereby high frequency noise removal efficiency, turbulent energy attenuation minimization and conservation of the main topological flow features were considered.

Velocity derivatives required in the calculation of the tensors S and Ω forming the symmetric and antisymmetric part of the velocity gradient tensor respectively (Eq.(1)) are inferred from differentiating the velocity field using a classical second order difference scheme. Compared with the fourth order accurate Hermitian scheme, it enables the minimisation of computational problems arising from noisy or over-sampled experimental data or from instantaneous velocity fields exhibiting abrupt flow directional changes.

2.2 *Extraction of swirling patterns*

The identification method applied in the present work starts with the detection of the position of vortex core centers by using the so-called λ_2 criterion [26]. A translational velocity is then estimated for every detected vortex core and is subtracted from the total field in which the vortex has been detected, before analysis of the topological features and energy content of all detected vortices.

2.2.1 *Location of vortex core centers*

Introduced by Jeong and Hussain (1995) [26], the λ_2 criterion has the two main properties which makes it interesting for coherent structures eduction: (1) to discriminate swirling and shearing motion (what is not achievable by visualizing only vorticity), (2) to be frame independent (meaning that vortex identification does not require the *a priori* choice of a reference frame to visualize the detected vortex cores). This criterion relies on the basic assumption that a vortex core centre is associated with the existence of a local pressure minimum. It is derived from the equation verified by the Hessian of pressure $\partial^2 p / \partial x_i x_j$, this quantity providing information about pressure extrema. The equation is obtained by applying the gradient operator on the Navier-Stokes equations [26]:

$$\frac{d}{dt}\left(S_{ij}\right) - \nu \frac{\partial^2 S_{ij}}{\partial x_k \partial x_k} + \Omega_{ik}\Omega_{kj} + S_{ik}S_{kj} = -\frac{1}{\rho}\frac{\partial^2 p}{\partial x_i \partial x_j} \tag{1}$$

where: $S_{ij} = \frac{1}{2}\left(\frac{\partial U_i}{\partial x_j} + \frac{\partial U_j}{\partial x_i}\right)$ is the component of the symmetric deformation rate tensor *S*,

$\Omega_{ij} = \frac{1}{2}\left(\frac{\partial U_i}{\partial x_j} - \frac{\partial U_j}{\partial x_i}\right)$ is the component of the antisymmetric spin tensor Ω.

Jeong and Hussain (1995) [26] attribute to the sum $\Omega_{ik}\Omega_{kj} + S_{ik}S_{kj}$ the occurrence of pressure minima due solely to coherent vortices. Denoting by $\lambda_1 \geq \lambda_2 \geq \lambda_3$ the three eigenvalues of this tensor, a variational analysis shows that pressure reaches a local minimum if and only if two of these eigenvalues are negative. The equivalent condition $\lambda_2 < 0$ was thus proposed for the definition of a vortex core. Vortices can subsequently be visualized by plotting iso-λ_2 contours.

Since our PIV velocity fields are two-dimensional, the full tensor $\Omega_{ik}\Omega_{kj} + S_{ik}S_{kj}$ cannot be formed. Instead, an equivalent two-dimensional form of this tensor has to be computed in the plane in which the PIV data lie. This is not completely rigorous insofar as the condition of a

zero divergence of velocity may be not necessarily fulfilled at every point of 2D instantaneous velocity vector field obtained by PIV (see Subsection 3.2.2).

In any of the instantaneous velocity vector field from where they are issued (Fig. 2a), the iso-λ_2 contour plots exhibit small-scale disturbances that arise from numerical noise (Fig. 2b). Therefore, λ_2 fields are first smoothed out by application of a two-dimensional homogeneous Gaussian filter with a size equal to 7×7 grid spacings (Fig. 2c). Even after filtering, the application of the λ_2-criterion on 2D vector fields still returns negative peaks of λ_2 that are not all relevant as some of them do not necessarily correspond to large values of the enstrophy field [24]. These peaks can easily be removed by setting a threshold and by retaining only the values of λ_2 such that $\lambda_2 < \lambda_{2,threshold}$ (Fig. 2d). This is what does our program, the difficulty lying in the choice of an appropriate value of the threshold. A rigorous sensitivity analysis was performed for filter type and size to find an adequate definition for $\lambda_{2,threshold}$, i.e. leading to the best identification of vortex core centers while being respectful of the flow physics [25]. Finally, the method used actually comes down to removing the values of λ_2 whose absolute value is lower than 40% of the absolute value $\left|\lambda_{2,\min}\right|$ of the absolute minimum of λ_2 calculated for the current instantaneous velocity field. The same percentage is applied to every snapshot regardless of the value of $\left|\lambda_{2,min}\right|$. The method was found in good agreement with the alternative criterion adopted by Schram et al (2004) [24, 25].

2.2.2 *Galilean transformation*

At this stage, the vortex core centers are detected. The iso-λ_2 contours previously determined can not be used to analyze the topological features of all detected vortices as a threshold is applied. This is the reason for which another way, based on the examination of the spatial distribution of velocity around the vortex center, is adopted to characterize geometrically the

structures (see Section 2.3).

This approach imposes that each detected vortex must be analyzed in a frame that moves at the same velocity as the core of the vortex [21, 27]. Therefore, the convection velocity of a vortex is estimated by the velocity measured at its center. It is then subtracted from the local instantaneous velocity field in which the vortex appears. Such a procedure assumes that the vortex is transported at a uniform velocity, which is not exactly true [25]. Note that in the experiments described further, the mean flow velocity in the region where most vortices were detected was almost zero and could be assumed uniform. The errors made in analyzing the detected vortices in reference frames moving at a uniform convection velocity was therefore neglected in first approximation.

2.3 *Vortex characteristics*

2.3.1 *Size and shape*

The size of a vortex is determined by examining the distribution of tangential component of velocity V_θ around the vortex centre. It is here assumed that a vortex core is marked by an increase in tangential component of velocity with radial position inside the vortex, and by a decrease in tangential component of velocity with radial position outside the vortex (Fig. 3a). Subsequently, the size and shape of a detected structure is estimated by numerically finding the maxima of V_θ along 8 directions defined by the angle they form with respect to the horizontal axis (Fig. 3b):

- 0° and 180° (horizontal direction, referred to as direction 1 or α=0°);
- 45° and 225° (first diagonal direction, referred to as direction 2 or α=45°);
- 90° and 270° (vertical direction, referred to as direction 3 or α=90°);
- 135° and 315° (second diagonal direction, referred to as direction 4 or α=135°).

The method relies on the filtered instantaneous velocity fields. In order to account for non-isotropic closed vortices, four diameters D_α (α=0°, 45°, 90°, 135°) are estimated for each

detected vortex from the sum of $R_{\alpha 1}$ and $R_{\alpha 2}$, the vortex radii defined as the distance to vortex centre from the point where, in the corresponding direction α, $|V_\theta|$ reaches a maximum (Fig. 3a). From this, it is inferred for each vortex:

- A mean diameter: $$D_m = \frac{1}{4} \sum_{\alpha=0,45,90,135} D_\alpha \quad (2)$$

- An eccentricity: $$\chi = \frac{max(\, D_\alpha \,)}{min(\, D_\alpha \,)} \qquad \alpha = 0°,45°,90°,135° \quad (3)$$

2.3.2 *Nature of structures*

Fig 3a represents the distribution of the tangential component of velocity distribution for an "ideal" closed circular vortex. In this case, there is no dependence of V_θ with radial position. In practice, many vortex cores do not exhibit such an ideal velocity distribution: this is the consequence of artificial topological distortions (approximate convection velocity) and/or of the physical deformations the structures undergo (stretching, compression, shear, misalignment with the normal to the measurement plane, lose of spatial integrity). Thus, several cases are distinguished:

- Case 1: the tangential velocity distribution of a swirling pattern is no more longer axisymmetrical but still presents a maximum whatever radial direction is considered. The radii $R_{\alpha 1}$ and $R_{\alpha 2}$ may vary with α, but the considered structure remains perfectly closed. Such a structure is referred to as a *closed vortex* or, more simply , a *vortex*.
- Case 2: a maximum of V_θ cannot be determined in one or more radial directions. Corresponding open structures are referred to as *vortices of first, second, third or fourth type* according to the number of open directions. The mean diameter of second, third and fourth type vortices is estimated without taking into account open directions. These directions are neither taken into account in the estimation of eccentricity. In the statistical analysis, open structures are considered separately.

2.3.3 *Energy content*

The vortical intensity I_V of a vortex core of surface area S_V is defined by

$$I_V = \Gamma / S_V \quad (4)$$

The circulation Γ is the vorticity flux across S_V:

$$\Gamma = \int_{S_v} \vec{\Omega} \cdot \vec{n} dS \quad (5)$$

where $\vec{n}$ is the external normal unit vector to the surface S_V, and $\vec{\Omega}$ denotes the vorticity vector that here reduces to $\Omega.\vec{n}$ with Ω the out-of-plane component of $\vec{\Omega}$. By applying Stokes theorem to the gridded PIV velocity data, Γ is estimated from:

$$\Gamma = \oint_{L_V} \vec{U} \cdot d\vec{l} \quad (6)$$

where L_V describes a closed path of integration along the surface S_V. Equation (6) is evaluated using the trapezoidal approximation. The path of integration is an ellipse centred at the position of the vortex core center and formed from both the minimum and maximum of D_α. A bi-linear interpolation of the velocity on this contour is performed. The vortical intensity I_V of a vortex core is finally obtained by dividing Γ by the surface area of the ellipse. It is interesting to note that the vortical intensity I_v of a vortex is a measure of frequency (s^{-1}) and can be associated with the revolution time of a vortex around its own axis [28]. When compared to the time scale representative of diffusive mechanisms occurring at the scale of the vortex core, I_v provides information about the spatial coherence of vortex.

2.4 *Statistical analysis*

The information below is stored in a database for each structure detected from series of instantaneous velocity fields:

- Number of the snapshot from which the structure was detected;
- Core centre coordinates;
- Diameters $D_{0°}$, $D_{45°}$, $D_{90°}$, $D_{135°}$, D_m and eccentricity χ;
- Rotation direction (according to the sign of vorticity at centre);
- Nature of the structure (closed vortex, vortex of first/second/third/fourth type),
- Circulation Γ and vortical intensity I_v.

From the large population of vortices educed on series of instantaneous velocity fields, the

probability density functions (pdf) of these quantities are computed. The percentage of vortices having a counter-clockwise/clockwise rotation direction is inferred as well as the two-dimensional probability distribution of presence of the detected vortices.

3. Application to the impingement region of air curtains

Firstly, details about experimental set-up, test configurations and PIV measurements are given. Some general characteristics about the flow topology in which the eddy structures are extracted are briefly presented in a second step. Finally, the results obtained with the vortex eduction method described above are examined.

3.1 *Experimental facility and instrumentation*

3.1.1 *Experimental set-up*

The experimental facility used in this study consists of a 6 m long horizontal open tunnel with a $0.3\ \mathrm{m} \times 1\ \mathrm{m}$ cross-sectional area. Only half of the whole set-up is schematically depicted in Fig. 4, the installation being symmetric geometrically. The front wall and the floor of the tunnel are transparent so as to allow PIV measurements. The floor-to-ceiling clearance can be varied in order to cover different values of the opening ratio H/e where H is the nozzle-to-plate distance and e is the nozzle width. The height of the air curtains considered in this study was constant and equal to 30 cm.

The blowing unit consists of two fully independent feeding circuits. It can be operated in single jet or twin-jet mode. The so-called exterior jet is always fed with air taken from the ambiance. The interior feeding circuit can be operated in a closed-loop mode to form a fully or partially recirculated air curtain. In this case, the interior jet is fed with air taken from inside the tunnel. The inlet section of the exterior feeding circuit is fitted with shutters so as to ensure a sufficient stability of the exit jet flow at low discharge velocities. Both feeding circuits comprise flow straighteners, filters and honeycombs in order to achieve uniform velocity profiles at the nozzle exit. The terminal diffuser has a 10:1 contraction ratio. The exit

section of the blowing unit is 0.03 m wide. It is divided into two nozzles of equal size by a 1.5 mm thick splitting plate. The discharged air streams are always blown vertically downwards, spanning the wind tunnel cross-section completely.

When the blowing unit is operated in the double jet mode, the initial velocity of each jet can be adjusted independently within the range of 1 m/s to 15 m/s by varying the rotation speed of the fans. A monitoring system consisting of 1.5 mm outer diameter total head tubes connected to standard micromanometers provides on-line information about outlet velocities, the signals from the pressure transducers being systematically recorded during measurements. The turbulence level at the nozzle exit is about 1%. From qualification and validation experiments, it was checked that the flow at the nozzle exit was highly uniform in the spanwise direction. No potential periodic component in the main flow caused by the fan vane passage frequency could be noticed under any circumstances.

3.1.2 *Test configurations*

Numerous experiments involving various air curtain arrangements have been performed in order to work out efficient solutions for ambiance confining [8, 25, 29]. In this paper, we restrict ourselves to considerations about three test-configurations involving only one air-curtain blown downwards transversally to the cross section of our tunnel. This air curtain was alternatively a single jet (SJ-SF), a double jet (or twin-jet) with both air circuits fed from the ambiance (DJ-SF, standing for Double-Jet Single-Flux) and a partially recirculated double jet (DJ-DF, standing for Double-Jet Double-Flux). These three different feeding and boundary conditions are illustrated in Fig. 5a, Fig. 5b and Fig. 5c, respectively. They have been explained in detail in [29]. For each configuration, three outlet velocities, U_0, at the nozzle exit were tested: 1, 3 and 7 m/s. In the case of double jets, both jets have the same outlet velocities. The associated Reynolds numbers are calculated by:

$$Re = \frac{U_o e}{\nu} \tag{7}$$

where e is the total width of the nozzle (e=1.5 cm for simple jet, e=3 cm for double jet).

In total, the vortex eduction method was applied to nine cases (three outlet velocities for each of the three air curtain configurations).

3.1.3 *PIV measurements*

Our eduction algorithm was applied to instantaneous velocity fields measured in about 6×6 cm^2 vertical x-z planes within the impingement region at the jet central plane (y/e=0) and at z=Z=36.5 cm from the front wall (Fig. 6). The dimensions of the observation window were chosen in accordance with the jet nozzle dimensions and with the expected size of the coherent structures possibly present in this flow region.

In the corresponding experiments, the flow was illuminated from below by a Quantel BrilliantB double cavity pulsed Nd:YAG laser operated at 532 nm. Each laser shot delivered up to 120 mJ with a pulse duration of 10 ns. The beam from the laser was passed through a series of spherical and cylindrical lenses to achieve a light sheet of thickness less than 1 mm. Digital images were recorded with a Kodak Megaplus ES 1.0 cross-correlation camera with a digital resolution of 1008 × 1016 pixels. The camera was fitted with a Nikon 1:2.8 28 mm lens that viewed the light sheet from a distance of about 15 cm. The PIV 2100 process unit and the FlowManager software from Dantec Dynamics A/S were used to record and analyze the images.

The seeding consisted of an aqueous glycerol solution and was produced by commercial smoke generators. It was delivered into the jet via both the primary jet air itself by injecting the particles upstream of the blowers and into the entrainment air by using appropriate multi-hole pipes suitably positioned in the far field on either side of the air curtain. Particle sizing of the smoke showed that 95 % of the particles had diameters below 5 µm. Table 1 presents the recording parameters of the PIV system.

Pairs of images were recorded at a rate of 15 Hz. The interrogation areas were cross

correlated. A Gaussian window function was applied to the interrogation areas to minimize phantom correlations near their edge. A subpixel interpolation scheme was used to resolve particle displacement to 1/64 of the pixel pitch on the CCD array. Peak-height, velocity range and moving-average validation procedures were applied successively after cross-correlation of the images. The percentage of spurious vectors rejected and substituted after application of the above validation procedures was 3 % on average. Typically, 400 to 500 pairs of images were recorded to ensure statistically convergent data sets.

3.2 *Overall view of the flow*

The aim of this section is to give an idea about the topology of the flow in which the eddy structures educed are embedded. For that, some general characteristics about the main flow (*x-y* plane) and about the mean flow in the wall region (*x-z* plane) are here presented respectively: the case of the twin-jet with simple flux and U_0=7 m/s is chosen for illustration in all the section. Note that the twin-jet flow comes close akin to the single jet flow, the main difference lying in the presence of Kármán-type vortices (at the interface between the two individual jets forming the air curtain) in the initial region of the main flow. These wake structures, which develop downstream of the nozzle splitting plate (see Fig. 7) vanish at a distance equal to about 5e.

3.2.1 *Flow in the x-y plane*

Fig. 7 provides a general picture of the main flow structure in the *x-y* plane. The dashed line located at *y/e*=0 in these figures shows the position of the *x-z* plane in which 2D-traces of coherent structures were subsequently sought for.

From Fig. 7a and Fig. 7b, it can be seen that the jet deviates slightly to the right. The stagnation line is located at *y/e*≈0.4. This has been attributed to the fact that the air curtain was not located at equal distance from the two far ends of the tunnel [29]. The two canonical jets forming the air curtain are clearly distinguishable in Fig. 7a. A closer look at the nozzle

exit velocity profiles would reveal almost top-hat profiles for each jet. The length of the potential core of each individual jet is close to 5*e*/2. Each jet exhibits an own potential core whose length is equal to what would be observed in the absence of the other jet. From *x/e*≈5 up to *x/e*≈8, the spatial distribution of mean velocity compares fairly well with the distribution obtained for a single impinging jet with the same opening ratio *H/e*.

By comparison with a single jet, the presence of a wake increases turbulence activity in the initial flow region between the two jets. However, the jet centre plane exhibits average turbulence levels much lower than within the two lateral shear layers that grow along the air-curtain outer boundaries where, apart from the impact region, most of the turbulent activity remains concentrated (Fig. 7c-7f). Within the impingement region, a relatively calm zone of average diameter about *e* exists. Maxima of turbulent kinetic energy are concentrated in a band that actually coincides with a stronger curvature of streamlines. In this region, the contribution of the fluctuations of the longitudinal and transverse components of velocity to the total amount of maximum turbulent kinetic energy is comparable.

3.2.2 *Flow in the x-z plane*

Fig. 8a represents contour plots of mean velocity magnitude (DJ-SF, U_0=7 m/s, *y/e*=0). In this nozzle symmetry plane, the flow is rather homogeneous in the *z*-direction. The mean flow velocity decreases almost linearly towards the impingement plane. Such results are representative of what can be observed in the other air curtain configurations.

Fig. 8b show the scalar field of $\partial\overline{U}/\partial x + \partial\overline{W}/\partial z = -\partial\overline{V}/\partial y$. Negative values indicate that the flow is accelerated towards the front end of the tunnel. The out-of-plane elongational strain decreases with distance from the impingement plate. The higher values lie in the region where most vortices have been detected, i.e. in a region whose depth is approximately equal to the nozzle width *e* (see further). Fig. 8b actually shows the degree of divergence of the considered mean velocity fields: the analyzed instantaneous velocity fields are not divergence

free.

3.3 *Results of vortex eduction method*

The results presented in the subsequent sections refer to closed vortices only (see Section 2.3.2). However, it should be noted that the tendencies described below would not be affected significantly by including open type vortices in the analysis.

3.3.1 *Vortex size and shape*

Typically, the total number of vortices detected is around 1500 for each case under test: on average, this corresponds to about four coherent structures on an instantaneous vector field. As shown in Fig. 9, almost 70 % of the detected structures are closed vortices while 25% correspond to first type open structures. This tendency seems to be sensitive neither to the outlet velocity nor to the air curtain configuration.

The probability density functions of D_m are plotted in Fig. 10. On average, the standard deviation of the probability density functions of D_m is equal to about 3.4 mm in any of the considered cases (Table 2). Fig. 10 reveals that, independently of the case, a broad range of structures coexist in the impingement region: most of the detected structures have their mean diameter comprised between 1.5 and 17.5 mm, i.e. between $e/20$ and $e/2$ (e being the total width of the jet nozzle, see Section 3.1.2). Our results confirm the numerical observations of [10, 30] who noticed the presence of isolated secondary vortex tubes of smaller diameter between vortex pairs of much larger importance. Unfortunately, because the integral computation time used in the corresponding numerical simulations was too low to consider proceeding to a statistically converged analysis of the observed structures, any comparison with our experimental results can only be limited.

For the three air curtain configurations, a maximum is reached for $D_m \approx 10$ mm at $U_0=1$ m/s, for $D_m \approx 6$ mm at $U_0=3$ m/s except for DJ-DF, and for $D_m \approx 4.5$ mm at $U_0=7$ m/s except for SJ-SF (Fig. 10).

As shown in Table 2, the median diameters (D_{median}) are systematically lower than the ensemble-averaged mean diameter ($\overline{D_m}$). For the three air curtain configurations, they are closer to 9 mm at U_0=1 m/s, to 8 mm at U_0=3 m/s and to 7 mm at U_0=7 m/s, corresponding to almost one fifth of the depth of the impingement region. At first sight, an increase in the outlet velocity would tend, independently of the configuration, to decrease slightly both the median and maximum diameter of the population of detected vortices.

As presented in Table 2 and in Fig. 11a, the ensemble-averaged value $\overline{D_m}$ of the pdf of D_m varies between 7.5 and 9.2 mm, i.e. between one quarter and one third of the total width of the nozzle jet. Apparently, this result is not in very good agreement with [31] who found $D_m \approx 0.6e$; however, a direct comparison is difficult as these authors characterized their vortices just by defining a sort of "height" inferred from the visual inspection of only one randomly chosen vortex pair observed in the case of a single jet. Considering the uncertainty in the determination of D_m, no significant effect of the configuration type on $\overline{D_m}$ can be definitely established (Fig. 11a). However, as for the two others characteristic diameters, the ensemble-averaged mean diameters decrease slightly with increasing outlet velocity at the nozzle jet. Such results would suggest that the vortex sizes are rather controlled by the Reynolds number.

In a similar way, the probability density function of eccentricity χ does not vary significantly with the case under test (Fig. 11b). For all cases, the ensemble-averaged values remain almost constant ($\overline{\chi} \approx 2$) as well as the median eccentricities closer to 1.7 (see Table 2); most of the detected vortices are characterized by an eccentricity ranging from 1 to 3. All these findings prove that the vortical patterns detected are elliptical rather than circular. A closer examination of the maximum and minimum diameters of the detected structures reveals that the ensemble-averaged diameters oriented at 0° and 90°, $\overline{D_{0°}}$ and $\overline{D_{90°}}$, are systematically

smaller that those oriented at 45° and 135°, $\overline{D_{45°}}$ and $\overline{D_{135°}}$ (Fig. 11a). Consistently with the results of [31], some preferential directions of deformations of the vortices seem thus to exist.

3.3.2 *Vortex rotation direction*

In Fig. 12, we have reported the percentage of vortices exhibiting either a clockwise or an counter-clockwise rotation. Globally, the fraction of vortices having a counter-clockwise rotation remains close to the fraction of vortices having a clockwise rotation. Thus, at first sight, our results tend to corroborate earlier observations [11, 31], putting forward the systematic presence of counter-rotating pairs or vortices in the impingement region of a plane turbulent jet.

A procedure was added to our program so as to check for the presence of counter-rotating structures in the immediate vicinity of any detected vortex. It was found that the eddy structures detected by our algorithm were not systematically organized in pairs of counter-rotating vortices: such pair patterns were not frequently observed. This was confirmed by a visual inspection of several velocity vector maps. This can actually be explained after consideration of what follows:

- The lifetime of the structures observed in the impingement region of our jets is generally much smaller than the time separating two consecutive snapshots. Therefore, the probability of detecting simultaneously the two eddy structures constituting a pair of counter-rotating vortices may not be equal to 1.
- The PIV measurement window used in the present experiments does not span entirely the width of our tunnel. We therefore cannot exclude the possibility of vortex pairs located at the edges of the measurement window where only one vortex would be visible.

Therefore, considering what precedes, we shall eventually refrain from drawing any premature conclusion that would unfairly question the results of [11, 31].

3.3.3 *Spatial distribution*

Representative examples of two-dimensional probability density function of presence of eddy structures are shown in Fig. 13. These distributions were simply obtained by counting the number of vortex centers detected in grid cells of dimension 3×3 mm^2 and by dividing by the total number of structures detected in the PIV observation window.

A high concentration of vortices is observed close to the wall. This would tend to demonstrate that the coherent structures present in the wall region of our jets do not originate from the upstream stream (from the main jet lateral mixing layers for instance) but rather arise in the impingement region. However, this statement should be considered with caution, as we cannot totally exclude the presence of structures in the process of formation in the upper part of our measurement window. If these evolving structures do not exhibit a sufficient degree of coherence and/or if their vorticity is too low, they can be missed by our algorithm.

Detected vortices are quite uniformly distributed horizontally. The absence of regularly spaced regions exhibiting peaks of density of presence tends to preclude both the possibility of particular channels through which vortices would travel and the likelihood of stationary swirling patterns. There is no indication of any tendency for vortices to form at preferential locations.

The cumulative probability density functions of presence plotted as a function of the wall distance shows that, for the twin-jet configurations, more than 80% of the detected structures are located within the lower half of the observation window, that is to say within a layer of depth equal to about e or $0.1H$. This coincides rather well with the wall region defined by [12] as a transition region between the confinement zone (where with respect to a free jet, the main flow entrainment and expansion rates decrease and increase, respectively) and the region where the flow separates into two opposite wall jets; these authors found that the wall

region was of the order of 13% of H.

According to Fig. 13a-13c, it can be noticed that the concentration of vortices in the vicinity of the wall is smaller in the case of simple jet configurations and that, for a configuration type, the Reynolds number has no significant influence.

3.3.4 *Vortex energy content and time scales*

The probability density functions of vortical intensity I_V are given in Fig. 14. Negative values refer to vortices rotating clockwise. All the distributions are roughly symmetrical and rather shew with a range that narrows with decreasing outlet velocities. Except for U_O=1 m/s, the I_v distributions tend to exhibit a positive and a negative extrema, corresponding to counter-clockwise and clockwise rotating vortices respectively. However, from this only, it cannot be concluded about the presence of counter-rotating vortex pairs.

For each case, the vortices rotating clockwise and counter-clockwise have about the same absolute value of the ensemble-averaged vortical intensity (Table 2). Higher vortical intensities $\overline{|I_V|}$ are obtained with twin-jets than with single jet, the use of a double flux system having no real influence. The $\overline{|I_V|}$ values vary significantly with outlet velocity: closer to 100-150 s^{-1} for U_0=1 m/s, they become equal to 300-450 s^{-1} for U_0=3 m/s and to 750-1200 s^{-1} for U_0=7 m/s. These findings reveal that the energy content of the eddy structures is mainly controlled by the Reynolds number. This is rather consistent with the decrease of the different characteristic diameters previously observed (see Subsection 3.3.1).

The values of I_V give an idea of the revolution time t_r of the detected structures around their own axis. In the present cases, t_r turns out to be of the order of 1 to 10 ms. Compared to the time that separates two successive pairs of PIV images (≈ 66.7 ms), it is now clearer why the present approach does not allow vortex coherence in time to be assessed.

The time scale t_d representative of diffusive mechanisms occurring at the scale of the vortex core can be calculated as $t_d \equiv R_v^2 / \nu_e$ where R_v denotes mean vortex radius, and ν_e is the

effective viscosity [28]. Taking a mean value of 8 mm for D_m and assuming a turbulent kinematic viscosity of the order of 100 times the molecular kinematic viscosity of air, the ratio t_d/t_r appears to be considerably larger than 1. This proves that diffusive mechanisms do not affect the thickness of a vortex core over several vortex revolutions [28] and thus, that a certain degree of spatial coherence can be attached to the structures detected here.

4. Conclusions

Reporting results from a broader research program dealing with ambience separation or confinement by air curtains, the present paper focuses on the flow structure in the impingement region of such jet systems . A vortex eduction method was developed to better understand the fashion in which the large-scale structures present in this flow region form, evolve and contribute to transfer mechanisms. Implemented in the Matlab environment, this method was designed to automatically detect and statistically characterize traces of spatially coherent eddy structures in 2D PIV velocity vector maps. The employed algorithm is primarily based on the λ_2 criterion of Jeong and Hussain (1995). This criterion is here used only to locate vortex core centers, the topological features of a structure being inferred from a local examination of the velocity field in a reference frame moving at the speed of the centre of this structure.

The method developed has been successfully applied on experimental data obtained from PIV measurements in the impingement region of three air curtain configurations (simple jet with simple flux, double jet with simple and double flux) and for three outlet velocities at the nozzle jet (1, 3 and 7 m/s). It was found that:

- Structures covering a wide range of sizes (from 1.5 to 17.5 mm) co-exist in this region.
- 70% of the structures detected are closed vortices and 25% are first type open structures.
- Most of eddies are concentrated close to the impingement plate, in a region whose depth does not exceed 3 % of the nozzle-to-wall distance. No specific location of vortices has

been observed: they are quite uniformly distributed horizontally.

- The fraction of vortices having a clockwise rotation direction remains close to the proportion of vortices having an counter-clockwise rotation direction. Nevertheless, the systematic presence of counter-rotating pairs of vortices could not been demonstrated.
- The vortices detected are predominantly ellipsoidal: some preferential directions of deformation have been identified.
- Their ensemble-averaged mean diameters vary between 7.5 and 9.2 mm. The maximum and median values of the D_m-pdf are significantly influenced by the Reynolds number, with the air curtain configuration having only slight impact. The vortical intensity of vortices is also very sensitive to the outlet velocity. Higher values have been obtained with double-jets than with a single jet. Finally, it is important to have in mind that an increase in outlet velocity tends to decrease vortex size and to increase their energy.

All these findings suggest that the coherent structures present in the wall region of air jets exist in connection with the streamline curvature imposed by the presence of the impingement plate, which is primarily a function of the opening ratio H/e. However, further experiments would be required to confirm that these structures do not have their origin in the mixing layers that develop along the lateral boundaries of the main flow.

In the future, additional studies will be performed to better understand the relationship between these coherent structures features and transfer mechanisms that control the sealing efficiency of air curtains.

Acknowledgements

The work presented in this paper was supported by the CNRS, the EMN and the French Embassy of New-Delhi (India) in the form of Post-doctoral and PhD grants. The authors are grateful to the technical staff (Mr Y. Gouriou, F.X. Blanchet and E. Chevrel) and S. Gupta who kindly provided us with the experimental data used in this work.

References

[1] J.I. Simper, New uses for air curtains, B.S.E. 43 (1975) A16-A18

[2] B. Etkin, W.D. McKinney, An air-curtain fume cabinet, AM. Ind. Hyg. Assoc. J. 53(10) (1992) 625-631

[3] J. Partyka, Analytical design of an air curtain, Int. J. Modelling and Simulation 15(1) (1995) 14-22

[4] M.A. Szatmary, Isolation chamber air curtain apparatus, Patent WO 98 50134 (1997)

[5] M. Pavageau, E.M. Nieto, C. Rey, Odour and VOC confining in large enclosures using air curtains, Water Sci. Tech. 44(9) (2001) 165-171

[6] S.C. Hu, Y.K. Chuah, M.C. Yen, Design and evaluation of a minienvironnement for semiconductor manufacture process, Build. Environ. 37 (2002) 201-208

[7] P. Bridenne, P. Coffinier, Procédé et dispositif pour diffuser un flux de protection à l'égard d'une ambiance environnante, Patent FR.2.824.626 (2002) Pontet et Alano SARL

[8] S. Gupta, M. Pavageau, C. Solliec, C. Rey, M. Dufresne de Virel, Particle Image Velocimetry measurements in air-curtain systems designed for smoke confining in the case of road tunnel fires, In Proc. of the 2nd Int. Conf. on Tunnel Safety and Ventilation, Graz Austria edited by P. Strurm and S. Minarek (2004) 127-134

[9] F. Beaubert, S. Viazzo, Large eddy simulation of plane turbulent impinging jets at moderate Reynolds numbers, Int. J. Heat and Fluid Flow 24 (2003) 512-519

[10] S. Yokobori, N. Kasagi, M. Hirata, Transport phenomena at the stagnation region of a two-dimensional impingement jet, Trans. JSME B 49(441) (1977) 1029-1039

[11] J. Sakakibara, K. Hishida, M. Maeda, Vortex structure and heat transfer in the stagnation region of an impinging plat jet (simultaneous measurements of velocity and temperature fields by digital particle image velocimetry and laser-induced

fluorescence), Int. J. Heat Mass transfer 40(13) (1997) 3163-3176

[12] S. Maurel, C. Rey, C. Solliec, M. Pavageau, Caractéristiques structurelles d'un jet d'air plan turbulent frappant une plaque plane placée à distance variable, Mécanique & Industries 5 (2004) 317-329

[13] K.B.M.Q. Zaman, F. Hussain, Turbulence suppression in free shear flows by controlled excitation, J. Fluid Mech. 103 (1981) 133-159

[14] F.B. Hsiao, J.M. Huang, On the dynamics of flow structure development in an excited plane jet, Trans ASME 116 (1994) 714-720

[15] S. Rajagopalan, N.W.M. Ko, Velocity and spanwise vorticity measurements in an excited mixing layer of a plane jet, Exp. Fluids 20 (1996) 346-357

[16] U. Vandsburger, C. Ding, Self-excited wire method for the control of turbulent mixing layers, AIAA J. 33(6) (1995) 1032-1037

[17] S. Rajagopalan, R.A. Antonia, Turbulence reduction in the mixing layer of a plane jet using small cylinders, Exp. Fluids 25 (1998) 86-103

[18] J.P. Bonnet, J. Delville, Coherent structures in turbulent flows and numerical simulation approaches, von Karman Institute for Fluid Dynamics Lecture Series 2002-04 on Post-Processing of experimental and numerical data (2002)

[19] F. Hussain, Coherent structures and turbulence, J. Fluid Mech. 173 (1986) 303-356

[20] M. Lesieur, Turbulence in fluids, Kluwer editions (1990)

[21] S.K. Robinson, Coherent motion in the turbulent boundary layer, Ann. Rev. Fluid Mech. 23 (1991) 601-639

[22] J.P. Bonnet, J. Delville, M.N. Glausner, R.A. Antonia, D.K. Bisset, D.R. Cole, H.E. Fiedler, J.H. Garem, D. Hilberg, J. Jeong, N.K.R. Kevlahan, L.S. Ukeiley, E. Vincendeau, Collaborative testing of eddy structure identification methods in free turbulent shear flows, Exp. Fluids 25 (1998) 197-225

[23] F. Scarano, Identification of coherent structures in turbulent flows based on Pattern Recognition Analysis, von Karman Institute for Fluid Dynamics Lecture Series 2002-04 on Post-processing of experimental and numerical data (2002)

[24] C. Schram, P. Rambaud, M.L. Riethmuller, Wavelet based eddy structure eduction from a backward facing step flow investigated using PIV, Exp. Fluids 36 (2004) 233-245

[25] M. Pavageau, K. Loubière, S. Gupta, Automatic eduction and statistical analysis of coherent structures in the wall region of a confined plane turbulent impinging jet, Exp. Fluids 41 (2006) 35-55

[26] J. Jeong, F. Hussain, On the identification of a vortex. J Fluid Mech. 285 (1995) 69-94

[27] S.K. Robinson, S.J. Kline, P.R. Spalart, Quasi-coherent structures in the turbulent boundary layer. Part II: verification and new information from a numerically simulated flat-plate boundary layer, in: Kline SJ, Afgan NH (ed) Near wall turbulence. Proceedings of Zaric Memorial Conference, New York Hemisphere (1989) 218-247

[28] P. Chassaing, Turbulence en mécanique des fluides: analyse du phénomène en vue de sa modélisation à l'usage de l'ingénieur, Collection Polytech INP Toulouse Cépaduès-Editions (2000)

[29] S. Gupta, Etude expérimentale du comportement dynamique et des performances de rideaux d'air en vue de la conception de systèmes de confinement cellulaire, PhD Report N°ED 03676-174, University of Nantes (2005)

[30] F. Beaubert, Simulation des grandes échelles turbulentes d'un jet plan en impact. PhD Report N°ED 0367-042 University of Nantes (2002)

[31] S. Maurel, C. Solliec, A turbulent plane jet impinging nearby and far from a flat plate. Exp. Fluids 31 (2001) 687-696

List of Tables

Table 1

Focal length lens (mm)	28
Numerical aperture	4
Field of view (mm^2)	60×60 ($2e \times 2e$)
Interrogation area size ($pixels^2$)	16 x 16
Interrogation area size (mm^2)	0.95×0.95 ($\approx e/30 \times e/30$)
Interrogation area overlap in both directions	50 %
Number of vectors in observation window	125×126
Spatial resolution of vector maps (mm)	0.489 ($\approx e/60$)
Number of vectors in vector maps	125×126
Pulse delay (μs)	30
Dynamic velocity range (m/s)	0.030:7.9
Accuracy with a 95% confidence level	±1%
Number of snapshots	≈450

Table 2

Air curtain configuration	U_0 (m/s)	D_m (mm)	χ	$I_{V\_\text{Clockwise}}$ (s^{-1})	$I_{V\_\text{Counter-clockwise}}$ (s^{-1})
SJ - SF	1	$\overline{D_m} = 8.4$ $D_{median} = 8.1$ $\sigma = 3.4$	$\overline{\chi} = 2.0$ $\chi_{median} = 1.7$ $\sigma = 0.7$	$\overline{I_v} = -117.1$ $\sigma = 78.4$	$\overline{I_v} = 122.5$ $\sigma = 76.8$
	3	$\overline{D_m} = 8.2$ $D_{median} = 7.7$ $\sigma = 3.5$	$\overline{\chi} = 2.1$ $\chi_{median} = 1.7$ $\sigma = 0.8$	$\overline{I_v} = -305.3$ $\sigma = 212.0$	$\overline{I_v} = 339.0$ $\sigma = 241.7$
	7	$\overline{D_m} = 8.1$ $D_{median} = 7.6$ $\sigma = 3.5$	$\overline{\chi} = 2.1$ $\chi_{median} = 1.7$ $\sigma = 0.8$	$\overline{I_v} = -740.0$ $\sigma = 504.0$	$\overline{I_v} = 761.6$ $\sigma = 516.9$
DJ - SF	1	$\overline{D_m} = 8.9$ $D_{median} = 8.8$ $\sigma = 3.4$	$\overline{\chi} = 2.0$ $\chi_{median} = 1.7$ $\sigma = 0.7$	$\overline{I_v} = -153.5$ $\sigma = 91.2$	$\overline{I_v} = 154.9$ $\sigma = 87.6$
	3	$\overline{D_m} = 8.3$ $D_{median} = 7.9$ $\sigma = 3.4$	$\overline{\chi} = 2.1$ $\chi_{median} = 1.7$ $\sigma = 0.8$	$\overline{I_v} = -443.9$ $\sigma = 315.5$	$\overline{I_v} = 459.0$ $\sigma = 297.6$
	7	$\overline{D_m} = 7.7$ $D_{median} = 6.9$ $\sigma = 3.5$	$\overline{\chi} = 2.1$ $\chi_{median} = 1.7$ $\sigma = 0.8$	$\overline{I_v} = -1199.4$ $\sigma = 890.3$	$\overline{I_v} = 1192.1$ $\sigma = 713.0$
DJ - DF	1	$\overline{D_m} = 9.2$ $D_{median} = 9.1$ $\sigma = 3.3$	$\overline{\chi} = 2.0$ $\chi_{median} = 1.6$ $\sigma = 0.7$	$\overline{I_v} = -99.5$ $\sigma = 59.8$	$\overline{I_v} = 94.9$ $\sigma = 59.8$
	3	$\overline{D_m} = 8.0$ $D_{median} = 7.5$ $\sigma = 3.4$	$\overline{\chi} = 2.0$ $\chi_{median} = 1.7$ $\sigma = 0.7$	$\overline{I_v} = -415.8$ $\sigma = 280.0$	$\overline{I_v} = 456.7$ $\sigma = 308.0$
	7	$\overline{D_m} = 7.5$ $D_{median} = 6.8$ $\sigma = 3.3$	$\overline{\chi} = 2.0$ $\chi_{median} = 1.6$ $\sigma = 0.8$	$\overline{I_v} = -1137.5$ $\sigma = 787.8$	$\overline{I_v} = 1086.0$ $\sigma = 721.62$

Figure Caption

Fig. 1 (a) Illustration of a plane turbulent jet profile

(b) Schematic representation of the eddy structures in the impingement region

Fig. 2 Location of vortex core centers (Z=0.365 m, H=0.3 m)

(a) An instantaneous velocity vector field issued from PIV and smoothed by a Gaussian filter (size: 7×7 grid spacings)

(b) The associated field of iso-λ_2 contours

(c) The λ_2-field smoothed by a Gaussian filter (size: 7×7 grid spacings)

(d) The λ_2-field smoothed and thresholded ($\lambda_{2,threshold} = 40\%\ \lambda_{2,min}$)

Fig. 3 **(a)** Profile of tangential component of velocity within the core of an ideal vortex

(b) Radial directions along which structure diameters were estimated

Fig. 4 Schematic view of the experimental apparatus

Fig. 5 Air curtain configurations under test

(a) Single Jet with Simple Flux (SJ-SF)

(b) Double Jet with Simple Flux (DJ-SF)

(c) Double Jet with Double Flux (DJ-DF)

Fig. 6 Position of the PIV measurement plane

Fig. 7 Mean flow characteristics in the x-y plane (DJ-SF U_0=7m/s)

(a) Mean velocity field

(b) Streamlines

(c) rms of the *x*-component of velocity

(d) rms of the *y*-component of velocity

(e) Reynolds stress

(f) Turbulent kinetic energy

Fig. 8 Mean flow characteristics in the x-z plane (DJ-SF, U_0=7m/s, y/e=0, z/e≈12)

(a) Mean velocity magnitude

(b) Mean velocity divergence $\partial\overline{U}/\partial x + \partial\overline{W}/\partial z$

Fig. 9 Fraction (%) of closed and open structures detected

Fig. 10 Probability density function of mean diameter of vortices

Fig. 11 **(a)** Ensemble-averaged values of D_m, $D_{0°}$, $D_{45°}$, $D_{90°}$ and $D_{135°}$ related to the vortices detected as a function of the test configuration

(b) Probability density function of eccentricity of vortices

Fig. 12 Percentage of vortices exhibiting a counter-clockwise or clockwise rotation direction

Fig. 13 Two-dimensional probability distribution of presence of vortices (x is here the distance from the wall and z is expressed in the reference of PIV observation window; all the figures have the same scales)

(a) SJ-SF 1 m/s

(b) SJ-SF 3 m/s

(c) SJ-SF 7 m/s

(d) DJ-SF 7 m/s

(e) DJ-DF 7 m/s

Fig. 14 Probability density function of vortical intensity of vortices

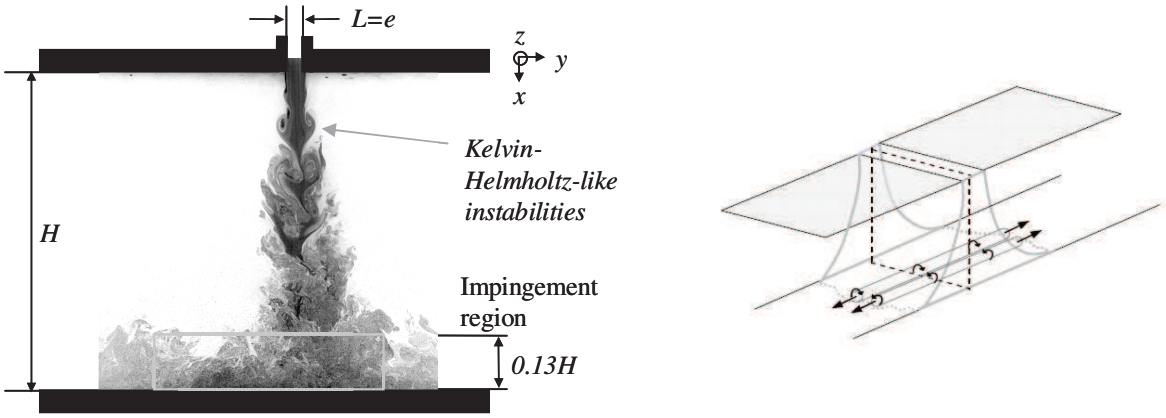
L=e
z
y
x
Kelvin-
Helmholtz-like
instabilities
H
Impingement
region
0.13H

(a) (b)

Fig. 1

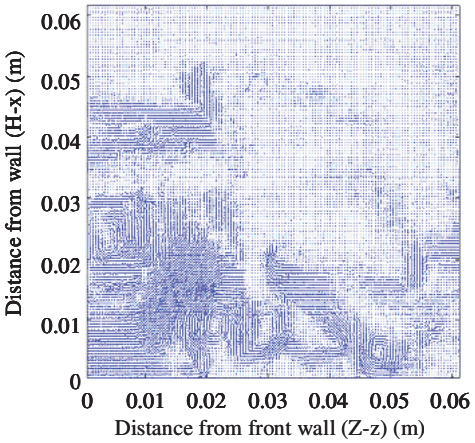
Distance from wall (H-x) (m)
0.06
0.05
0.04
0.03
0.02
0.01
0
0 0.01 0.02 0.03 0.04 0.05 0.06
Distance from front wall (Z-z) (m)

(a)

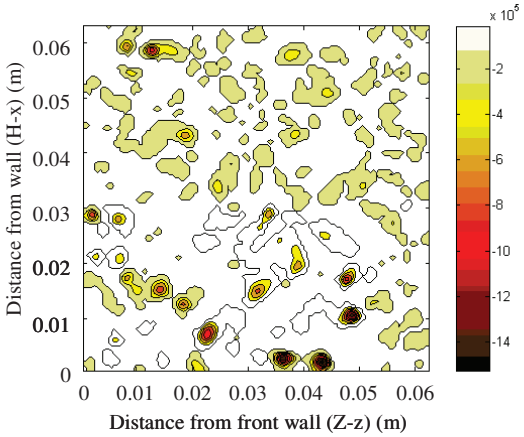
x 10^-5
-2
-4
-6
-8
-10
-12
-14
Distance from wall (H-x) (m)
0.06
0.05
0.04
0.03
0.02
0.01
0
0 0.01 0.02 0.03 0.04 0.05 0.06
Distance from front wall (Z-z) (m)

(b)

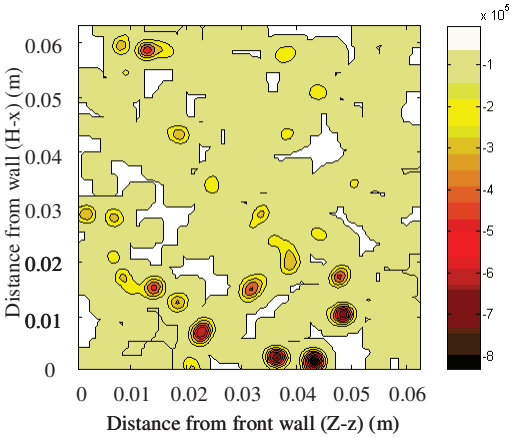
x 10^-5
-1
-2
-3
-4
-5
-6
-7
-8
Distance from wall (H-x) (m)
0.06
0.05
0.04
0.03
0.02
0.01
0
0 0.01 0.02 0.03 0.04 0.05 0.06
Distance from front wall (Z-z) (m)

(c)

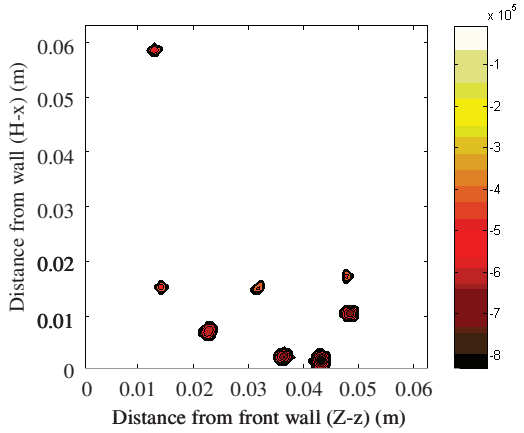
x 10^-5
-1
-2
-3
-4
-5
-6
-7
-8
Distance from wall (H-x) (m)
0.06
0.05
0.04
0.03
0.02
0.01
0
0 0.01 0.02 0.03 0.04 0.05 0.06
Distance from front wall (Z-z) (m)

(d)

Fig. 2

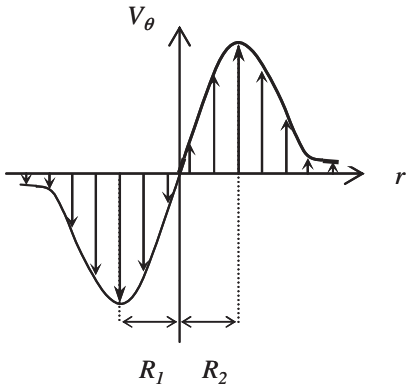

(a)

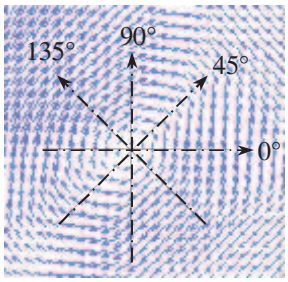

(b)

Fig. 3

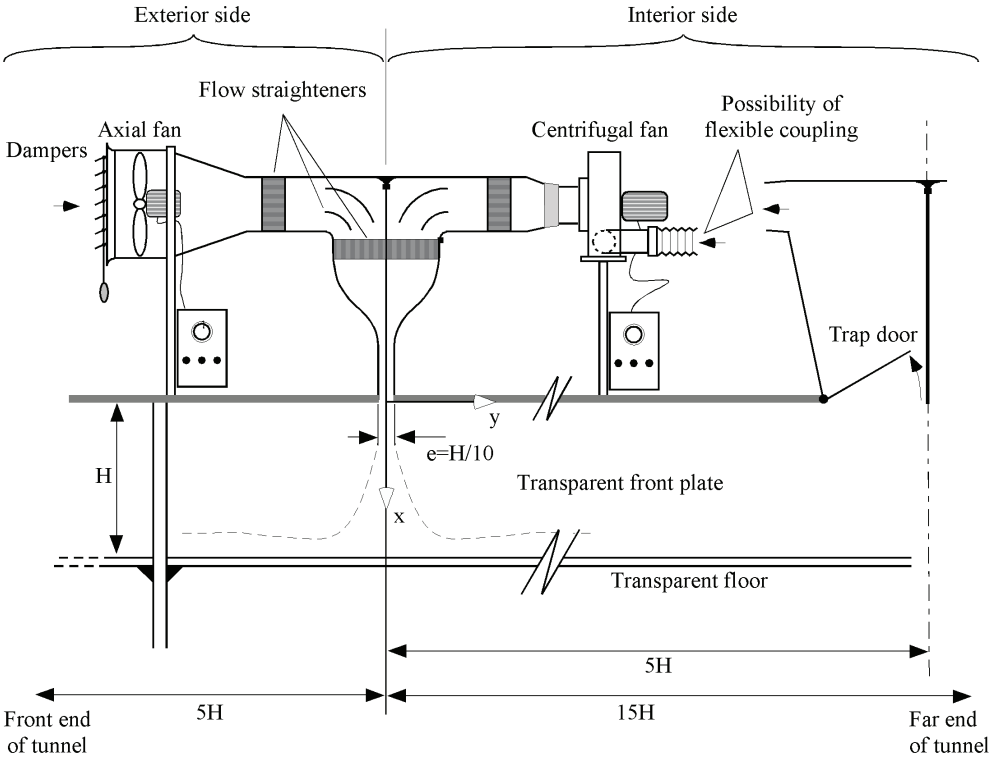
Exterior side
Interior side
Flow straighteners
Axial fan
Dampers
Centrifugal fan
Possibility of
flexible coupling
Trap door
y
e=H/10
H
Transparent front plate
x
Transparent floor
5H
5H
15H
Front end
of tunnel
Far end
of tunnel

Fig. 4

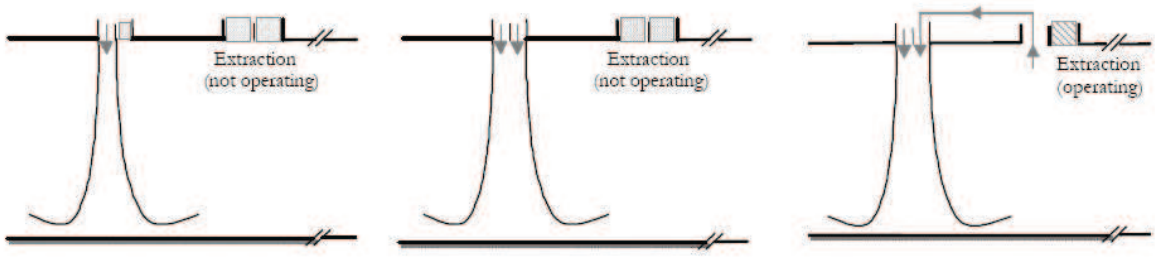
Extraction
(not operating)
Extraction
(not operating)
Extraction
(operating)

(a) *(b)* *(c)*

Fig. 5

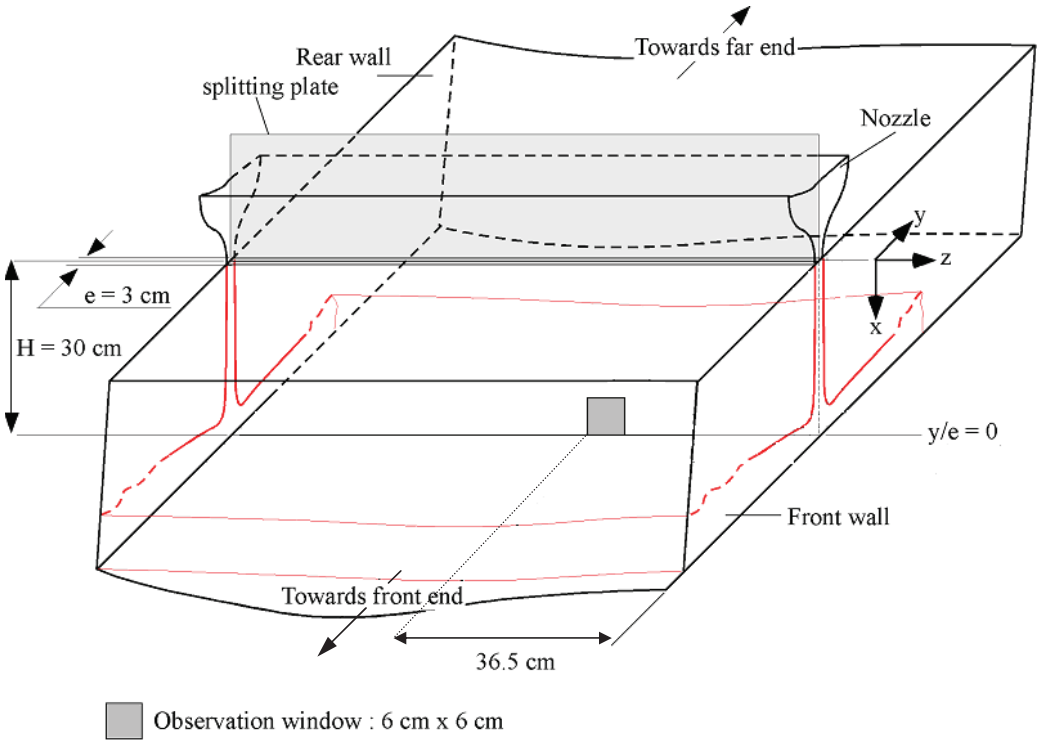
Towards far end
Rear wall
splitting plate
Nozzle
y
z
x
e = 3 cm
H = 30 cm
y/e = 0
Front wall
Towards front end
36.5 cm
Observation window : 6 cm x 6 cm

Fig. 6

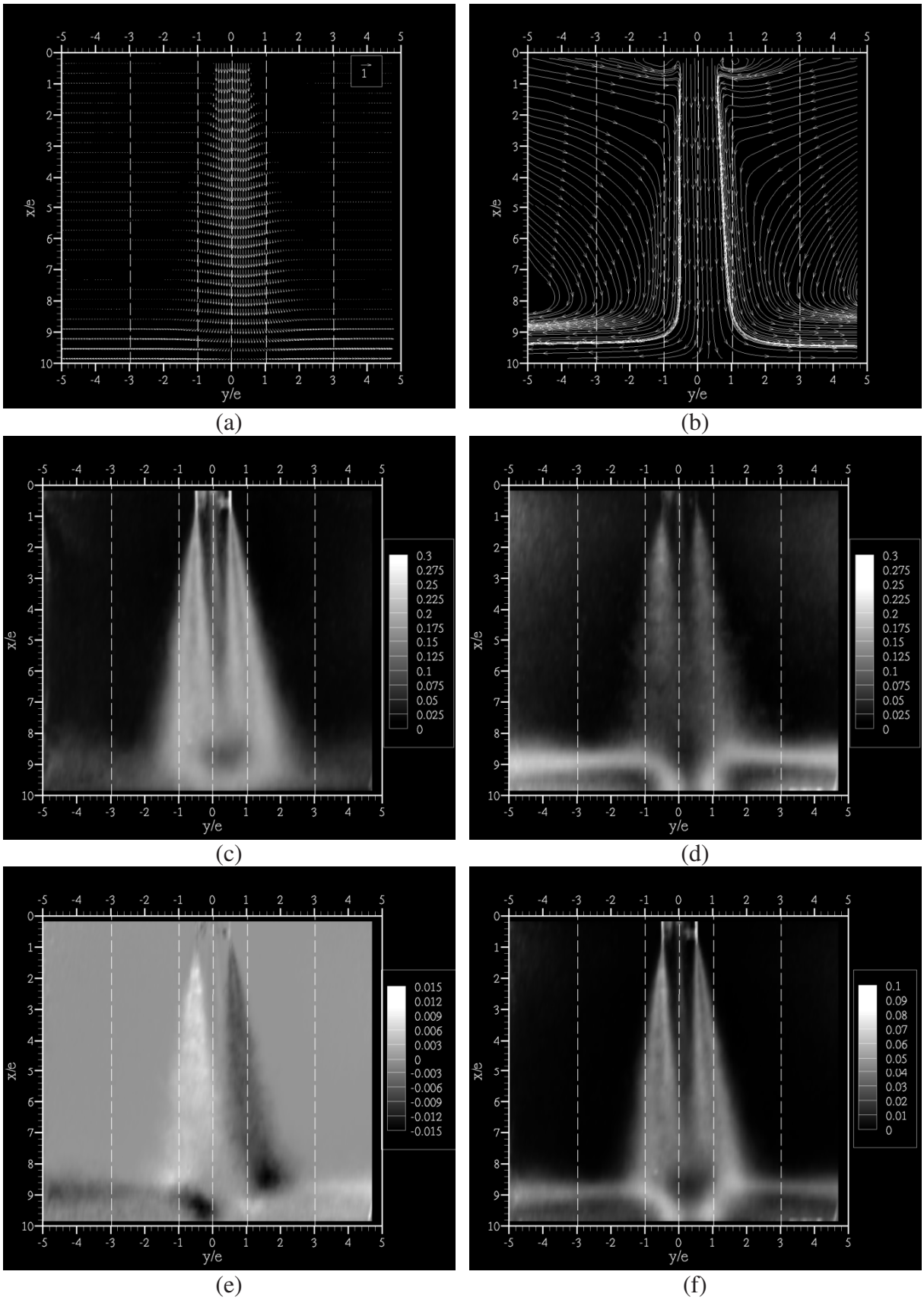

Fig. 7

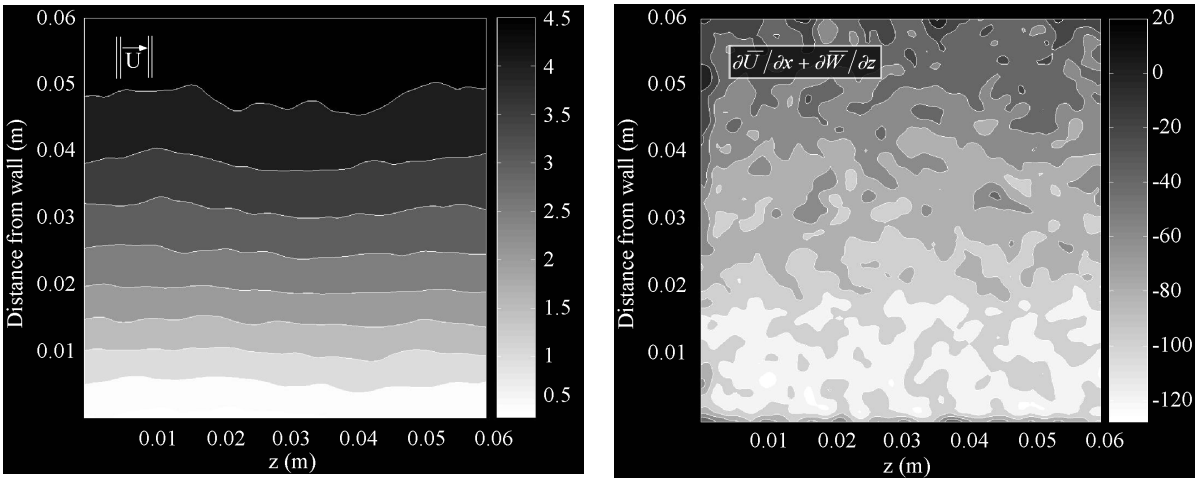
0.06
0.05
0.04
0.03
0.02
0.01
Distance from wall (m)
$\|\vec{U}\|$
4.5
4
3.5
3
2.5
2
1.5
1
0.5
0.01 0.02 0.03 0.04 0.05 0.06
z (m)
$\partial\overline{U}/\partial x + \partial\overline{W}/\partial z$
20
0
-20
-40
-60
-80
-100
-120

(a) *(b)*

Fig. 8

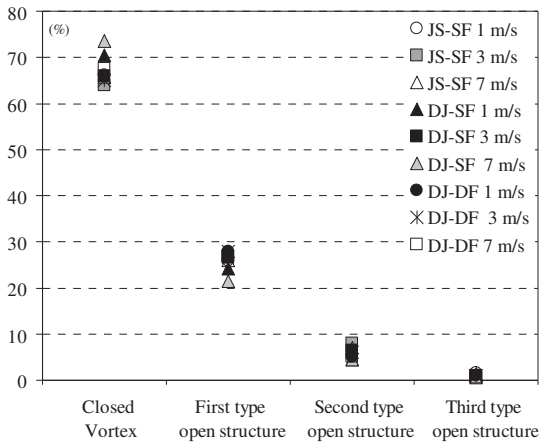
80
70
60
50
40
30
20
10
0
(%)
JS-SF 1 m/s
JS-SF 3 m/s
JS-SF 7 m/s
DJ-SF 1 m/s
DJ-SF 3 m/s
DJ-SF 7 m/s
DJ-DF 1 m/s
DJ-DF 3 m/s
DJ-DF 7 m/s
Closed Vortex
First type open structure
Second type open structure
Third type open structure

Fig. 9

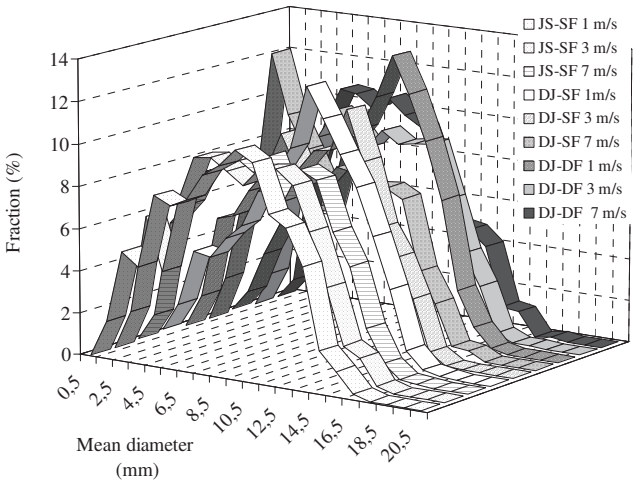
JS-SF 1 m/s
JS-SF 3 m/s
JS-SF 7 m/s
DJ-SF 1m/s
DJ-SF 3 m/s
DJ-SF 7 m/s
DJ-DF 1 m/s
DJ-DF 3 m/s
DJ-DF 7 m/s
Fraction (%)
0
2
4
6
8
10
12
14
0,5
2,5
4,5
6,5
8,5
10,5
12,5
14,5
16,5
18,5
20,5
Mean diameter
(mm)

Fig. 10

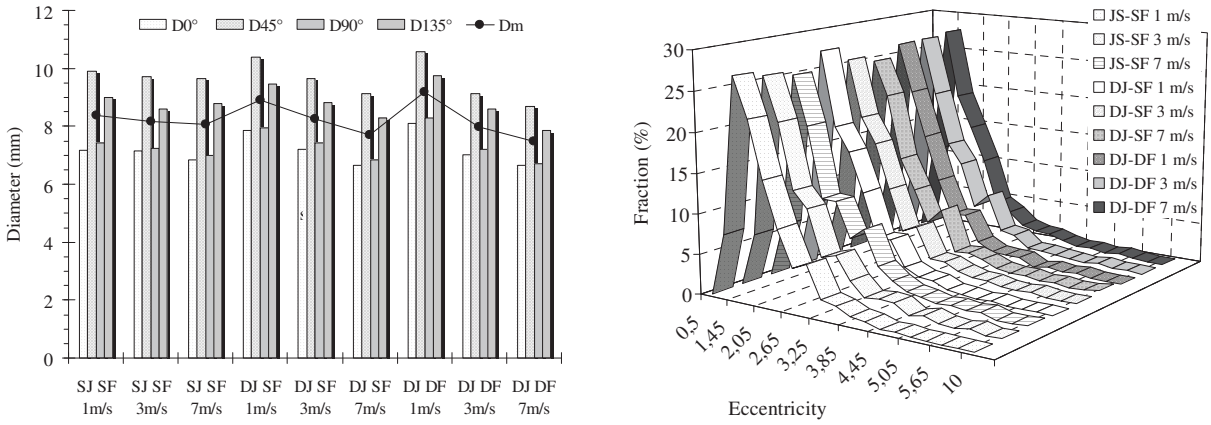
D0°
D45°
D90°
D135°
Dm
Diameter (mm)
12
10
8
6
4
2
0
SJ SF 1m/s
SJ SF 3m/s
SJ SF 7m/s
DJ SF 1m/s
DJ SF 3m/s
DJ SF 7m/s
DJ DF 1m/s
DJ DF 3m/s
DJ DF 7m/s
JS-SF 1 m/s
JS-SF 3 m/s
JS-SF 7 m/s
DJ-SF 1 m/s
DJ-SF 3 m/s
DJ-SF 7 m/s
DJ-DF 1 m/s
DJ-DF 3 m/s
DJ-DF 7 m/s
Fraction (%)
30
25
20
15
10
5
0
0,5
1,45
2,05
2,65
3,25
3,85
4,45
5,05
5,65
10
Eccentricity

(a) ***(b)***

Fig. 11

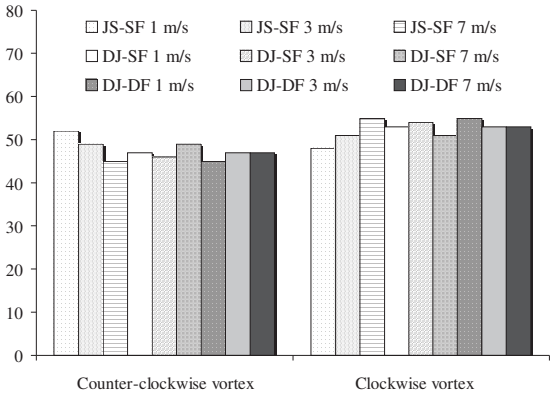
80
70
60
50
40
30
20
10
0
JS-SF 1 m/s
JS-SF 3 m/s
JS-SF 7 m/s
DJ-SF 1 m/s
DJ-SF 3 m/s
DJ-SF 7 m/s
DJ-DF 1 m/s
DJ-DF 3 m/s
DJ-DF 7 m/s
Counter-clockwise vortex
Clockwise vortex

Fig. 12

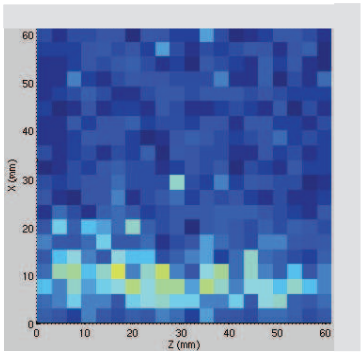

(a)

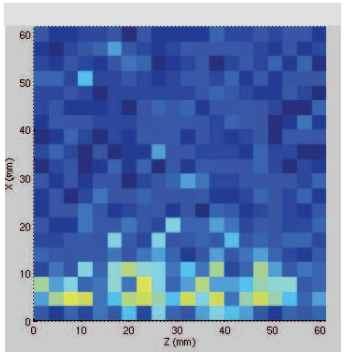

(b)

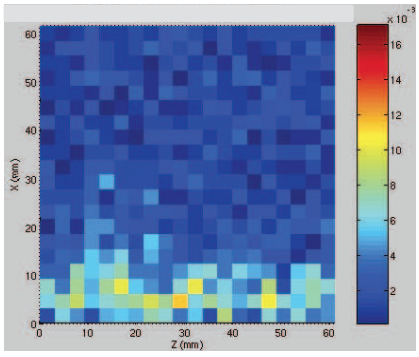

(c)

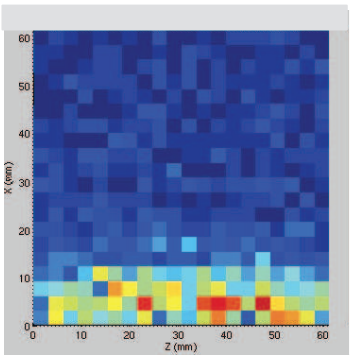

(d)

Fig. 13

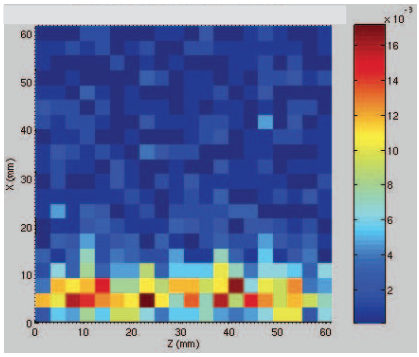

(e)

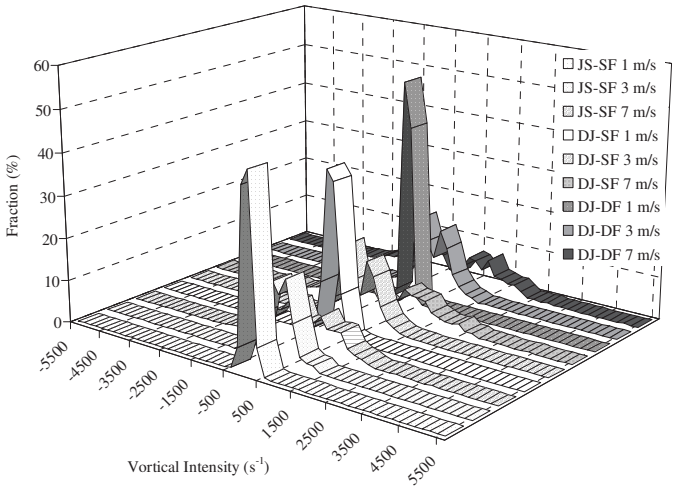
Fraction (%)
60
50
40
30
20
10
0
-5500
-4500
-3500
-2500
-1500
-500
500
1500
2500
3500
4500
5500
Vortical Intensity (s-1)
JS-SF 1 m/s
JS-SF 3 m/s
JS-SF 7 m/s
DJ-SF 1 m/s
DJ-SF 3 m/s
DJ-SF 7 m/s
DJ-DF 1 m/s
DJ-DF 3 m/s
DJ-DF 7 m/s

Fig. 14